ACS MEASUREMENT SCIENCE Au
AN OPEN ACCESS JOURNAL OF THE AMERICAN CHEMICAL SOCIETY

pubs.acs.org/measureau
Article

Methods for Tomographic Segmentation in Pseudo-Cylindrical Coordinates for Bobbin-Type Batteries

Dominick P. Guida, Alyssa M. Stavola, Andrew Chihpin Chuang, John S. Okasinski, Matthew T. Wendling, Xiaotong H. Chadderdon, and Joshua W. Gallaway*

Cite This: ACS Meas. Sci. Au 2023, 3, 344–354
Read Online
ACCESS | Metrics & More | Article Recommendations

ABSTRACT: High-resolution X-ray computed tomography (CT) has become an invaluable tool in battery research for its ability to probe phase distributions in sealed samples. The Cartesian coordinates used in describing the CT image stack are not appropriate for understanding radial dependencies, like that seen in bobbin-type batteries. The most prominent of these bobbin-type batteries is alkaline Zn−MnO_2, which dominates the primary battery market. To understand material radial dependencies within these batteries, a method is presented to approximate the Cartesian coordinates of CT data into pseudo-cylindrical coordinates. This is important because radial volume fractions are the output of computational battery models, and this will allow the correlation of a battery model to CT data. A selection of 10 anodes inside Zn−MnO_2 AA batteries are used to demonstrate the method. For these, the pseudo-radius is defined as the relative distance in the anode between the central current collecting pin and the separator. Using these anodes, we validate that this method results in averaged one-dimensional material profiles that, when compared to other methods, show a better quantitative match to individual local slices of the anodes in the polar θ-direction. The other methods tested are methods that average to an absolute center point based on either the pin or the separator. The pseudo-cylindrical method also corrects for slight asymmetries observed in bobbin-type batteries because the pin is often slightly off-center and the separator often has a noncircular shape.

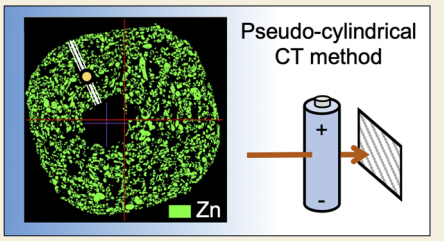

KEYWORDS: *alkaline battery, cylindrical battery, zinc anode, zinc oxide, X-ray tomography, battery CT*

INTRODUCTION

Batteries have become an integral part of society across many industries, from consumer electronics to electric vehicles. As more performance is demanded from these systems, advanced visualization techniques such as X-ray computed tomography (CT) and scanning electron microscopy (SEM) have been employed to better understand and develop future battery technology.[1−5] Owing to its low cost, inherent safety, and high energy density, the alkaline Zn−MnO_2 chemistry has dominated the primary battery market for decades.[6,7] Zn−MnO_2 has a smaller share in the rechargeable battery market compared to Li-ion due to its poorer cyclability.[8] The common bobbin-type Zn−MnO_2 batteries (AA, AAA, etc.) employ electrodes much thicker than that seen in rechargeable Li-ion batteries, maximizing the amount of active material present within each cell.[8,9] Development of new forms of rechargeable alkaline Zn−MnO_2 has also received attention as a possible candidate for grid-scale energy storage.[10−12]

Within a bobbin-type alkaline Zn−MnO_2 battery, an anode composed of irregularly shaped Zn particles suspended in a gelled KOH electrolyte is situated in the center of a cylindrical steel casing. The geometry and construction of a cell are shown in Figure 1a, as well as the definition of the r−θ plane in cylindrical coordinates. Between the anode and the steel casing is the MnO_2 cathode, which is isolated from the anode by a separator. This separator acts as an electronic insulator to prevent the battery from shorting internally while permitting ion transport between the electrodes. The cathode is electronically connected to the positive terminal via the conductive steel casing, while the anode is connected to the negative terminal via a brass pin.[8] This brass pin is in theory situated in the center of the anode; however, in practice, it does not always align perfectly with the battery center. This leads to the brass pin being off-center when the cell is viewed as a cross section in the r−θ plane. Additionally, the manufacturing process leads to a slightly squared-off anode shape due to the method for assembling the separator strips. Because current travels from anode to cathode current collectors, this means the current path is not of equal length across the anode at all θ values.

Received: April 1, 2023
Revised: May 22, 2023
Accepted: May 23, 2023
Published: June 21, 2023

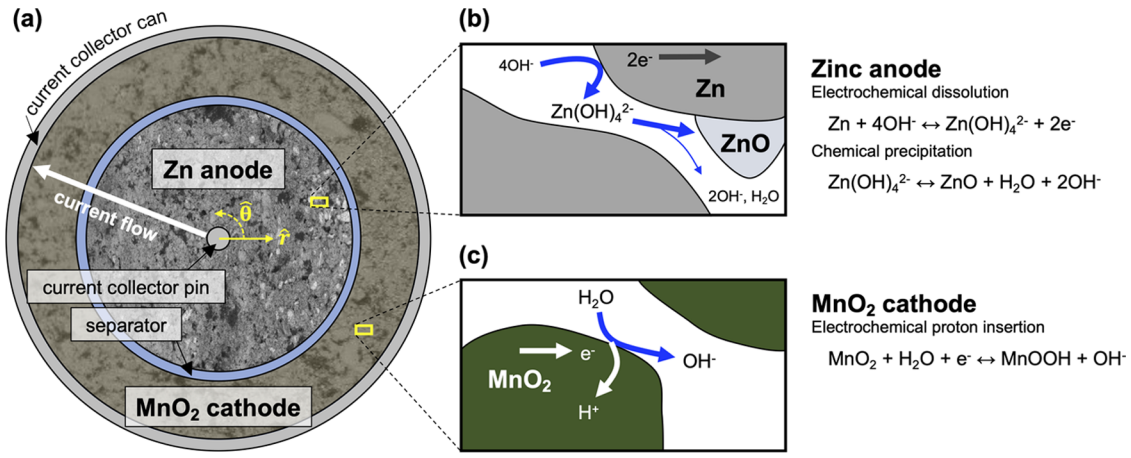

Figure 1. (a) Geometry of a bobbin-type cylindrical Zn−MnO_2 battery. (b) Schematic representation of the microstructure and discharge reactions of the Zn anode. (c) Schematic representation of the microstructure and discharge reactions of the MnO_2 cathode.

We have recently published a study correlating cylindrical Zn−MnO_2 CT results to calculations from a one-dimensional (1D) battery model.[13] A cylindrical 1D battery model assumes that the battery has material and discharge variations only in the *r*-direction. Effectively, this means the battery is averaged in the θ-direction and *z*-direction. This presents a challenge when averaging the CT data because various θ-directions of the anode can have different radii, depending on the placement of the pin and the shape of the separator. In this work, we present a method for transforming CT data to pseudo-cylindrical coordinates. Using a selection of 10 AA batteries with various discharge histories, we also demonstrate quantitatively that this pseudo-cylindrical coordinate method results in averaged 1D material profiles for the cell's entire data set that match individual cell slices better than alternative averaging methods. The cell anodes are used for this comparison because discharged anodes have large material variations, containing Zn, ZnO, and pore.

Figure 1b shows the discharge reactions in the Zn anode. During discharge, hydroxide is consumed in the anode as Zn dissolves into the electrolyte via eq 1, producing zincate and liberating two electrons[14,15]

$$Zn + 4OH^- \leftrightarrow Zn(OH)_4^{2-} + 2e^- \quad (1)$$

The KOH electrolyte is the hydroxide source during discharge, where the ionic flux is directed radially inward to sustain the dissolution of Zn. The electrons produced from the dissolution of Zn similarly move radially inward, leaving the anode via the brass current collecting pin. As discharge continues, the electrolyte can become supersaturated with zincate, prompting the formation of solid ZnO via eq 2.[16,17] If hydroxide is depleted, the formation of ZnO can occur from the direct oxidation of Zn, shown in eq 3[18]

$$Zn(OH)_4^{2-} \leftrightarrow ZnO + H_2O + 2OH^- \quad (2)$$

$$Zn + 2OH^- \leftrightarrow ZnO + H_2O + 2e^- \quad (3)$$

The formation of ZnO has been shown to be highly spatially dependent, particularly along the thickness of the anode.[19] Given that the formation of ZnO is associated with a volumetric expansion of the solid phase, this will lead to a reduction of pore space. This impedes hydroxide transport as the electrolyte-filled pore space is the ionically conductive phase.[19,20] Furthermore, ZnO is significantly more electronically resistive than Zn, meaning its formation leads to an overall decrease in ionic and electronic conductivities throughout the anode.[8,20] A reduction in either ionic or electronic conductivity may degrade battery performance and can lead to premature cell failure. It is therefore imperative to properly characterize the spatial dependence of ZnO within these batteries.

Figure 1c shows the proton-insertion reaction that initially occurs in the cathode until side reactions are triggered by a higher depth of discharge (DOD). The focus of this work is the anode, where the formation of the ZnO phase has a large impact on battery performance. In eq 4, a proton is inserted into the MnO_2 crystal lattice, coupled to the generation of OH^-

$$MnO_2 + H_2O + e^- \leftrightarrow MnOOH + OH^- \quad (4)$$

Of the many modern characterization techniques that have been employed in battery research, CT is uniquely advantageous. By relying on the transmission of high-energy X-rays, CT can be performed with no special sample preparation.[9] The technique involves processing measured radiographs with a reconstruction algorithm, producing a 3D representation of the sample. The resulting grayscale values of the voxels are based on the X-ray attenuation of the materials present within the sample. By using CT, the internals of a hermetically sealed battery can be probed to determine electrode properties such as phase distribution, porosity, and morphology. This technique has been used as such in many battery chemistries, including Zn−air,[2,21] Zn−MnO_2,[1,13,22,23] and Li-based[4,5,24] systems.

Although CT experiments are qualitatively informative through visual inspection of the produced image stack, it is desirable to extract quantitative results as well. Image segmentation is frequently used with CT data to discretize greyscale images into the phases present within the sample. Strategies for segmentation within batteries are predominantly either histogram-based[2,22,25] or machine-learning[5,26,27] methods. The resulting segmented CT data has been used to understand the phase distribution in batteries based on Cartesian coordinates.[5,21,28,29] Though this is appropriate for planar electrodes, its effectiveness in batteries with cylindrical symmetry is questionable. For some batteries with a cylindrical form factor, Cartesian coordinates remain appropriate due to the overall direction of the current flow. For example, a button-

https://doi.org/10.1021/acsmeasuresciau.3c00015
ACS Meas. Sci. Au 2023, 3, 344−354

type Zn−air battery has a cylindrical form but with an assumed symmetry in the angular and radial dimensions.[2] This is because the air cathode is located on the bottom of the battery, rather than around its circumference. As the axial dimension is identical for both Cartesian and cylindrical coordinates, analyses in Cartesian coordinates are thus still well-suited for Zn−air button cells. However, bobbin-type and jelly-rolled batteries do not display a radial symmetry but rather have notable radial dependencies that cannot be adequately described by analyses in Cartesian coordinates.[19,30,31]

To capture radial profiles from CT data that is in Cartesian coordinates, the equivalent cylindrical coordinates must be estimated. This so-called pseudo-cylindrical system should include the approximate radial and angular position relative to a central reference point. Radial profiles could then be obtained from CT data for systems that are more aptly described in cylindrical coordinates. This is particularly vital for bobbin-type alkaline Zn−MnO_2 batteries, as they employ thick electrodes in the radial dimension, displaying highly heterogeneous behavior along the radius.[19]

Within batteries, it is well established that the relative ease of ionic and electronic conductions in an electrode is highly relevant. Specifically, inhomogeneity in electrode utilization is largely dependent on the effective ionic and electronic conductivities.[32,33] As a result, it is important to consider the ion and electron sources and sinks when analyzing an electrode. In the case of commercial Zn−MnO_2 batteries, this complicates radial analyses if the current collecting pin is off-center. This disrupts the cylindrical symmetry of the cell and should be considered when developing a pseudo-cylindrical analysis.

Obtaining accurate radial profiles for bobbin-type batteries from experimental CT results is critical for developing computational models. Alkaline Zn anodes have frequently been described using 1D macrohomogeneous models, predicting the radial behavior of these systems from the current collector to the separator.[34−37] To compare these predictions with experimental results, similar radial profiles spanning from the current collector to the separator must be calculated from the CT data. This is important not only to validate the accuracy of a given model but also to guide further model development.

EXPERIMENTAL SECTION

Sample Cylindrical Battery Preparation

The samples analyzed by CT were commercial AA batteries produced by Energizer. The AA batteries were approximately 50 mm in height and 14 mm in diameter. The central anode was composed of Zn particles and had a height of approximately 42 mm and a diameter of 8 mm. The annular MnO_2 cathode had an inner diameter of 9 mm and an outer diameter of just under 14 mm. The capacity of these cells measured by slow discharge was 2820 mA h, as reported previously.[13] The pristine anode of an undischarged battery consisted of irregularly shaped Zn particles surrounded by pores filled with KOH electrolyte. After the discharge reaction began, ZnO would also be present in the anode because ZnO is the discharge product from eqs 2 and 3. Batteries were discharged to a given DOD in mA h using either a pulsed or continuous discharge protocol prior to imaging and are summarized in Table 1. The pulsed discharge procedures were as follows: the 50 mA cells were discharged for 1 h followed by a 7 h rest (50 mA h per 8 h); the 250 mA cells were discharged for 1 h followed by a 23 h rest (250 mA h per 24 h); the 750 mA cells were discharged for 2 min followed by a 58 min rest, and this cycle was repeated for 8 h per 24 h (200 mA h per 24 h). These three pulsed protocols are established ANSI tests for AA alkaline batteries. A detailed analysis of the difference between continuous and pulsed discharge results has been reported previously.[13] An analysis of Zn and ZnO distribution profiles in cells 1−10 as a function of discharge conditions is a topic of future work, while the focus of this work is on the analytical method itself.

Table 1. Summary of the Discharge Conditions for the 10 Commercial AA Energizer Batteries Tested

cell ID	cell symbol	discharge protocol	discharge rate (mA)	DOD (mA h)	pin distance from center (μm)
1	+	pristine	0	0	157
2	●	continuous	50	710 (25%)	209
3	★	continuous	50	1420 (50%)	57
4	▼	pulsed	50	1420 (50%)	296
5	◆	continuous	250	710 (25%)	266
6	▲	continuous	250	1420 (50%)	105
7	■	pulsed	250	1420 (50%)	122
8	▶	continuous	750	710 (25%)	110
9	◀	continuous	750	1420 (50%)	183
10	★	pulsed	750	1420 (50%)	183

Battery X-ray Computed Tomography (CT)

The data used in developing a process to convert Cartesian-based CT image stacks into pseudo-cylindrical coordinates was obtained at beamline 6-BM-A at the Advanced Photon Source (APS) at Argonne National Laboratory, where the experimental setup was as depicted in Figure 2. A high-flux polychromatic X-ray beam from the synchrotron source was the incident beam on the sample. The transmitted X-ray beam was converted to visible light via a scintillator, reflected off a mirror, magnified through a lens, and recorded by a camera. Each sample was rotated 360°, where projection data was collected at 0.1° intervals. The voxel resolution was 2.93 μm/voxel. The resulting data was reconstructed by a Gridrec algorithm to get a 3D representation of the battery.[38] The polychromatic X-ray beam was 4.5 mm wide and 1.5 mm high. The top and bottom of the beam were trimmed so that the axial height probed was 1.172 mm. This was assumed to be representative of the overall battery due to axial symmetry. The 3D volume probed was at 1/3 of the battery total height. This height was chosen to avoid any end effects at the top or bottom of the battery. The trimmed incident beam was thus 4.5 mm × 1.172 mm, and this defined one field of view (FOV). To capture data on the full diameter of the battery, which was larger than 4.5 mm, multiple overlapping FOVs were stitched. The method for stitching FOVs has been reported previously.[13]

When conducting CT experiments, there is a trade-off between FOV, voxel resolution, and data collection time. By stitching a small number of FOVs, a volume of approximately 200 mm^3 could be probed in a reasonable time frame of 380 min. This covered the full battery diameter of 14 mm and a height of 1.172 mm along the z-axis. (It should be noted that this refers to the z-axis of cylindrical coordinates, not the z-axis of the APS coordinate system, which is different.) In some other cells, the anode only was probed by centering the FOV entirely within the battery interior, dropping data collection time to 180 min.

CT Data Segmentation

The reconstructed image stack produced by the synchrotron CT experiment was segmented to identify the discrete phases present in the sample. These segmented CT images were then false-colored to more easily identify different phases, a 3D example of which is shown in Figure 3a. In this segmentation, the undischarged Zn is green, the solid ZnO is purple, and pore is black (transparent). The segmentation process included noise reduction efforts through the statistical region merging algorithm developed by Nock and Nielsen, as well as a Gaussian smoothing filter.[39] A complete description of the segmentation algorithm used has been reported previously.[13]

https://doi.org/10.1021/acsmeasuresciau.3c00015
ACS Meas. Sci. Au 2023, 3, 344−354

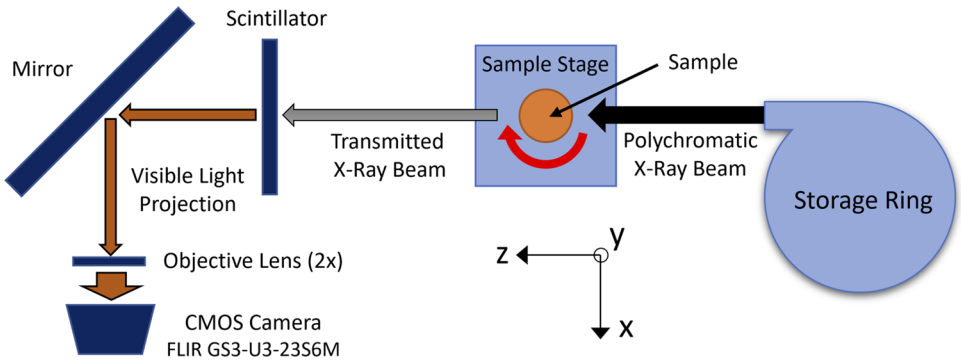

Figure 2. Diagram of the setup for CT experiments at beamline 6-BM-A at Argonne National Laboratory. The axes shown are the APS coordinate system, which was different than the coordinate system used in subsequent battery analysis.

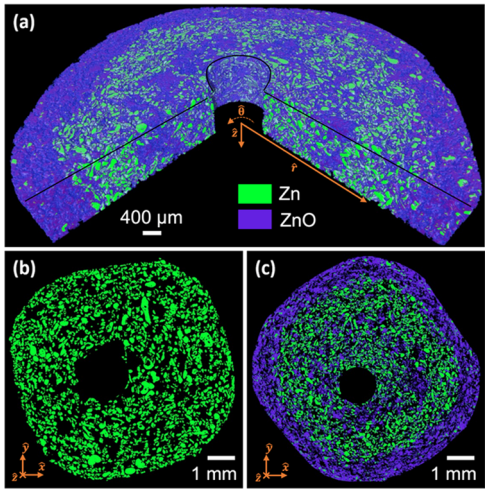

Figure 3. Segmented Zn−MnO_2 X-ray CT results. (a) Segmented 3D volume of an AA anode pulse discharged at 750 mA to 1420 mA h (cell #10). The data has been cut away to show the interior, and a black line has been added to visually define the edge. (b) Cross section of a pristine AA anode (cell #1). (c) Cross section of the same AA anode shown in panel (a) (cell #10).

Terminology Used in the Analysis

The spatial terminology used is defined in Figure 4. The height probed in the z-direction was 1.172 mm. The voxel size was 2.93 μm/voxel. This means 400 cross sections of 2.93 μm height were obtained. These cross sections could also be referred to as z-slices and were one voxel high in the z-direction. To analyze homogeneity in the polar θ-direction, cross sections were divided into θ-slices, which resembled a slice of pie. This is illustrated in Figure 4a. The choice of eight θ-slices per cross section was arbitrary but sufficient to assess material variations. The multiple cross sections stacked in the z-direction formed a 3D volume, shown in Figure 4b.

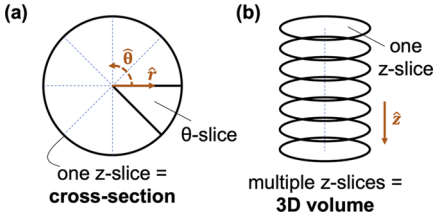

Figure 4. Terminology used in the analysis. (a) A single anode cross section, which is a 2.93 μm high slice along the battery z-direction or z-slice. To analyze homogeneity in the polar θ-direction, cross sections were divided into θ-slices. (b) A data set for one anode contained 400 cross sections. These stacked along the battery z-direction to form a 3D volume. The total height probed was thus 1.172 mm.

RESULTS AND DISCUSSION

Figure 3a shows a segmented 3D volume of a AA battery anode discharged to 1420 mA h (50% DOD) by pulsed galvanostatic discharge at 750 mA (2 min on per hour). The full data set of 1.172 mm height is shown. Segmented CT data is useful because individual material phases are identified based on their electron densities. In this way, the volume fractions of the anode materials—Zn, ZnO, and KOH electrolyte—can be known as a function of location in the anode. To correlate segmented CT results to calculations from a 1D battery model, the θ- and z-directions were averaged to obtain phase volume fractions as a function of r. This was done by first averaging a single cross section of the anode across all values of θ. Then, all of the cross sections were averaged along z. Two examples of cross sections are shown in Figure 3b,c. Figure 3b shows a pristine anode, containing only Zn and electrolyte-filled pores. Figure 3c shows a single cross section of the same discharged anode as Figure 3a. This consequently had a ZnO discharge product also distributed throughout the anode. A single cross section had a thickness of 2.93 μm, determined by the voxel size.

Definition of Pseudo-Cylindrical Coordinates

Considering the cross section in Figure 3b, each pixel within this image is extended in the third dimension to produce a cubic voxel, whose value indicates the material present at that voxel's location. Given the grid-like structure of a collection of cubic voxels, CT data is naturally described by Cartesian coordinates, as shown by the coordinate axes. However, this becomes problematic for samples that are better described by cylindrical coordinates.[7] A method to represent this information radially was desired.

The most straightforward method of converting a voxel's position (x,y) to radial coordinates was measuring the absolute distance from the center of the battery. However, given that the current collecting pin was not perfectly centered, the absolute distance could be measured using either the separator or the current collecting pin as a reference point. The cross sections shown in Figure 5 were made by placing the four sides of the panels at the center of the separator. Then, the separator and cathode were masked, and the pin was masked, so only the anode remained. The center of the anode could be defined based on the location of the separator, which defined its outer edge. This was approximately the center of the panel, shown by

https://doi.org/10.1021/acsmeasuresciau.3c00015
ACS Meas. Sci. Au 2023, 3, 344−354

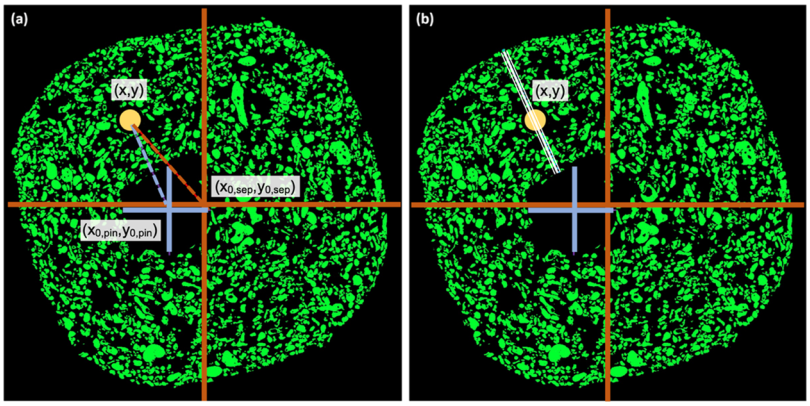

Figure 5. Methods for determining the radial position of a voxel at (x,y) marked with an orange circle. The centers of the pin $(x_{0,pin},y_{0,pin})$ and separator $(x_{0,sep},y_{0,sep})$ are marked with blue and red lines. The size of the orange circle is exaggerated for viewing. (a) Measuring the absolute distance from either the current collecting pin or center of the separator. (b) Measuring the relative position between the current collecting pin and the edge of the anode (marked by the tripled white line).

the crossing red lines and denoted by $(x_{0,sep},y_{0,sep})$. Alternatively, the center of the anode could be defined based on the location of the current collecting pin, which defined its inner edge. The center of the current collecting pin, shown by the crossing blue lines, was denoted by $(x_{0,pin},y_{0,pin})$. These methods are illustrated in Figure 5a. The problem with these methods is that the direction of the current flow across the anode is along a pseudo-radius from the surface of the current collecting pin to the surface of the current collecting can. In reality, the current follows a tortuous path, but the gradients that drive the current are along this pseudo-radius. The resistances that govern nonuniform reaction are a function of the distance traveled along this pseudo-radius. Neither choice of reference point, $(x_{0,sep},y_{0,sep})$ nor $(x_{0,pin},y_{0,pin})$, faithfully represents this. As an example, points that are equal distances from the pin $(x_{0,pin},y_{0,pin})$ could possibly have different distances from the separator. An analogous argument applies for choosing $(x_{0,sep},y_{0,sep})$ as the reference. Our hypothesis for this work was that for a large majority of cases, the important position was instead the relative distance between the pin and the separator.

The desired coordinate definition for any given voxel is the relative position between the current collecting pin and the separator. This is shown as a point along the tripled white line in Figure 5b. The relative distance along this pseudo-radius can be calculated using the reference points $(x_{0,sep},y_{0,sep})$ and $(x_{0,pin},y_{0,pin})$ defined previously. We demonstrate below that anode discharge characteristics match well for different θ-slices when compared using this relative distance. In other words, radial phase profiles for Zn and ZnO in discharged anodes are most often a function of the relative distance between the electron sink (center pin) and ion source (separator/cathode), even in cases where the current collecting pin is off-center.

The angular position for a voxel at (x,y) relative to the separator and the current collecting pin can be defined by eqs 5 and 6. The arctangent function in these equations is the four-quadrant inverse tangent, returning the angle relative to zero radians

$$\theta_{sep} = \tan^{-1}\left(\frac{y_{0,sep} - y}{x_{0,sep} - x}\right) \times \frac{180^\circ}{\pi} \tag{5}$$

$$\theta_{pin} = \tan^{-1}\left(\frac{y_{0,pin} - y}{x_{0,pin} - x}\right) \times \frac{180^\circ}{\pi} \tag{6}$$

Though symmetry in θ is assumed, calculating θ will allow the validity of that assumption to be verified. The distance between a voxel and the centers of the anode and current collecting pin can be calculated by eqs 7 and 8, respectively

$$d_{sep} = \sqrt{(x_{0,sep} - x)^2 + (y_{0,sep} - y)^2} \tag{7}$$

$$d_{pin} = \sqrt{(x_{0,pin} - x)^2 + (y_{0,pin} - y)^2} \tag{8}$$

The trajectory of the voxel relative to the center of the current collecting pin, m, is calculated via eq 9, which, for visual purposes, is the slope of the tripled white line in Figure 4b

$$m = \frac{y_{0,pin} - y}{x_{0,pin} - x} \tag{9}$$

With the voxel's trajectory relative to the center pin known, an iterative process is used to identify the distance between the center pin and the separator along that trajectory, which is used to find the relative position of the voxel between the pin and the separator. This iterative process begins by taking steps in the x and y dimensions along the pin-voxel trajectory, described in eqs 10 and 11, respectively. Within these two equations, i is used to indicate the iteration number

$$x_i = x_{i-1} + \alpha_{i-1} \times \frac{x - x_{0,pin}}{|x - x_{0,pin}|} \tag{10}$$

$$y_i = y_{i-1} + \alpha_{i-1} \times m \times \frac{x - x_{0,pin}}{|x - x_{0,pin}|} \tag{11}$$

Equations 10 and 11 involve a sensitivity parameter, α_{i-1}, that dictates the step size in the two dimensions. This sensitivity parameter begins at unity and decreases an order of magnitude every time the iteration overshoots or undershoots the separator, described in eqs 12 and 13. During the iteration process, the sensitivity parameter is adjusted by β to allow the iterative process to converge. The value of β depends on γ, which represents the error of a given iteration from the desired answer

https://doi.org/10.1021/acsmeasuresciau.3c00015
ACS Meas. Sci. Au 2023, 3, 344−354

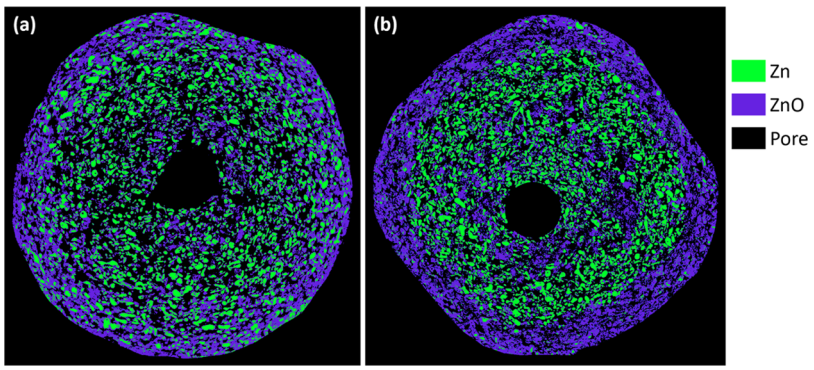

Figure 6. Cross sections of segmented CT data with false-colored phases. (a) Anode continuously discharged at 250 mA to 1420 mA h (cell #6), with a current collecting pin that was 105 μm off-center. (b) Anode pulse discharged at 750 mA to 1420 mA h (cell #10), with a current collecting pin that was 183 μm off-center.

$$\alpha_i = \begin{cases} \alpha_{i-1}\cdot(-10)^{\beta_i},\ i > 0 \\ 1,\ i = 0 \end{cases} \tag{12}$$

$$\beta_i = \begin{cases} 0,\ \dfrac{\gamma_i}{|\gamma_i|} = \dfrac{\gamma_{i-1}}{|\gamma_{i-1}|} \\ -1,\ \text{otherwise} \end{cases} \tag{13}$$

Equation 12 acts to reduce the sensitivity parameter each time the current iteration surpasses the correct answer without dropping below the error threshold. That is, the distance between an iteration's coordinates, (x_i,y_i), and the center of the separator will equal the radius of the separator once the iterative process has located the edge of the anode. This value, shown in eq 14, represents the error of a given iteration in finding the edge of the anode along the current trajectory. Specifically, γ is the difference between the radius of the anode, r_{sep}, and the distance from the center of the anode to the position of the current iteration

$$\gamma_i = \sqrt{(x_{0,sep} - x_i)^2 + (y_{0,sep} - y_i)^2} - r_{sep} \tag{14}$$

This iterative process continues until γ_i is below 10^{-3} microns, where it can then be reasonably assumed the edge of the anode has been identified and labeled as (x_{end},y_{end}). The distance between the center pin and the edge of the anode for the current trajectory, defined by δ, is computed using eq 15. Therefore, δ can be used with the radius of the current collecting pin, r_{pin}, and the voxel's distance from the center of the current collecting pin, d_{pin}, to calculate the pseudo-cylindrical radial position of the voxel, $\hat{r}$, using eq 16

$$\delta = \sqrt{(x_{0,pin} - x_{end})^2 + (y_{0,pin} - y_{end})^2} \tag{15}$$

$$\hat{r} = \frac{d_{pin} - r_{pin}}{\delta - r_{pin}} \tag{16}$$

Radial Volume Fraction Profiles in Pseudo-Cylindrical Coordinates

Two partially discharged anodes with current collecting pins at differing distances from the center of the anode can be seen in Figure 6. The figure is of the segmented CT results of these batteries that have been false-colored, where Zn is green, ZnO is purple, and KOH-filled pore is transparent. The battery in Figure 6a has a current collecting pin that is 105 μm from the center of the anode, while the one in Figure 6b has a current collecting pin that is significantly further from the center of the anode at 183 μm. Our purpose is to compare the analysis of volume fractions in these cells using the pseudo-cylindrical coordinate method presented above in Figure 5b. This will be compared to the more direct methods in Figure 5a. The goal is the faithful representation of CT data in a way appropriate for comparison to a 1D battery model, in which volume fractions are given as a function of battery radius, with symmetry assumed in θ and z. The batteries in Figure 6 were discharged by different profiles: Figure 6a was discharged continuously and Figure 6b was discharged with a pulsed profile. We have reported previously that pulsed discharge results in a ZnO formation near the current collecting pin, while continuous discharge results in the largest concentration of ZnO at the separator.[13] We have previously shown that 1D battery models predict continuous discharge results well, but pulsed discharge results are more challenging to predict.[13] Especially for data with a highly off-center pin such as that in Figure 6b, it is important to establish how the data should be compared to 1D modeling data.

The radial profiles of the segmented phases were computed via the three methods described in Figure 5: two absolute methods based on both the pin and separator centers and also the pseudo-cylindrical method. That is, $\hat{r}$, d_{sep}, and d_{pin} were all used to calculate the distinct radial volume fraction profiles. One would predict that, by definition, these three methods for a battery with a perfectly centered pin would have no difference. By extension, these methods should deviate from each other as the current collecting pin is further from the center of the anode.

It is typically assumed that there is homogeneity along the height of the battery, which is the z-direction in both Cartesian and pseudo-cylindrical coordinates. As such, the radial position computed from eq 16 for a given (x,y) can be applied to all values of z. This allows the entire 3D volume measured by CT to be included in calculating the radial profiles. Though the cross sections featured in this work only show a single z-slice along the height of the battery, the reported radial profiles encompass the entire portion of the 3D volume that was measured by CT. We assume homogeneity in the z-direction, but if this were not the case, the z-direction could be treated as an additional independent variable, creating distribution profiles that varied as a function of both radius and height.

A comparison of the radial results for the cells in Figure 6 using the three previously defined methods is shown in Figure

https://doi.org/10.1021/acsmeasuresciau.3c00015
ACS Meas. Sci. Au 2023, 3, 344−354

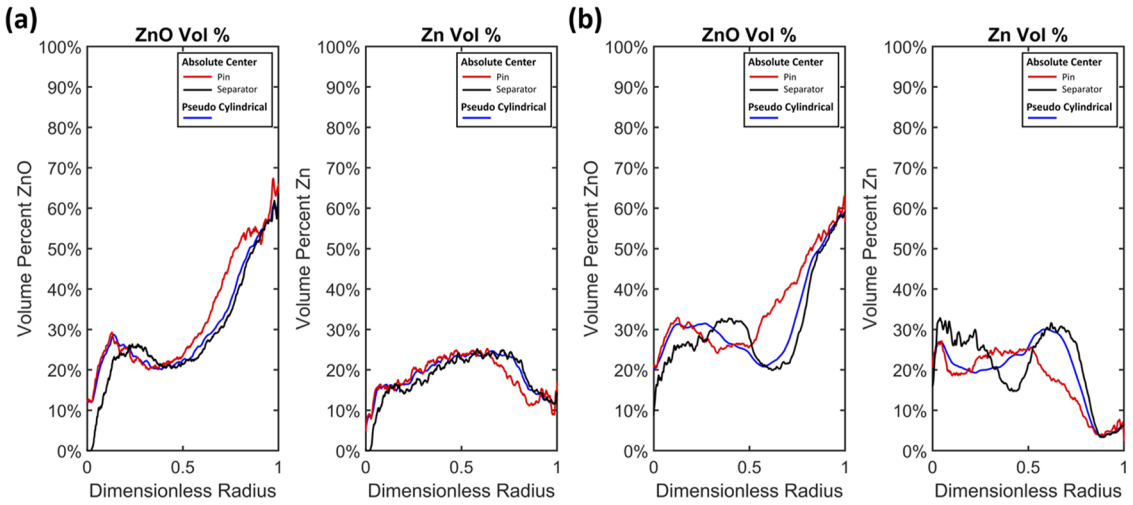

Figure 7. Radial volume fraction profiles for Zn and ZnO within partially discharged anodes, using the three methods described in Figure 5. (a) The anode in Figure 6a (cell #6), with a current collecting pin slightly off-center. (b) The anode in Figure 6b (cell #10), with a current collecting pin significantly off-center.

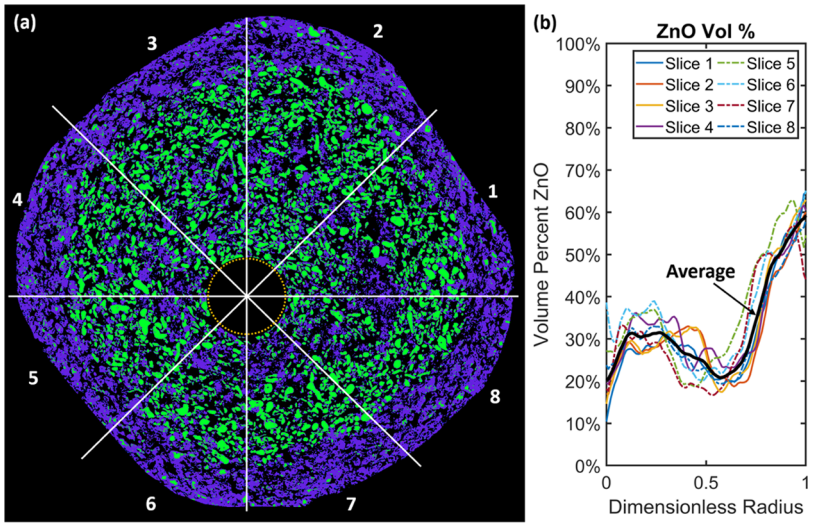

Figure 8. Segmented θ-slices of a partially discharged anode. (a) False-colored segmented CT data for a battery pulsed discharged at 750 mA to 1420 mA h (cell #10), annotated to show eight θ-slices. (b) Smoothed 1D radial volume fraction profile of ZnO for each of the eight θ-slices and their average.

7. As expected, for anodes with a current collecting pin nearly centered in the anode, the three methods resulted in radial ZnO and Zn profiles that were approximately the same, shown in Figure 7a. This was a result of the battery having a current collecting pin sufficiently close to the center of the separator to mimic the true cylindrical symmetry. For the cell in Figure 7a, ZnO had the greatest volume fraction near the separator (nearly 65%, at a dimensionless radius of 1) and the least at the pin (dimensionless radius of 0). The Zn profile had a maximum of 24% in the middle of the anode. Less Zn was at the separator because the highest local discharge rate was there. The reduced Zn fraction at the pin was an artifact due to small voids around the pin where the anode contacts it. The essential agreement between the three methods used to calculate the profiles was an important conclusion.

However, the same could not be said for the battery in Figure 7b, which had a current collecting pin significantly further from the center of the separator. This battery's radial profiles differed substantially depending on the method used to compute them, as seen in Figure 7b. The Zn profiles calculated based on the separator center and by the pseudo-cylindrical method looked somewhat similar, having a local maximum near 30% located about a third of the distance from the separator. However, the method based on the pin only showed a broad maximum of half the distance from the separator. This was caused by the inner ring of the undischarged Zn in Figure 6b being very different distances from the off-center pin depending on the radial θ value. The ZnO profiles calculated by all three methods showed a ZnO "crust" around the perimeter of the anode (at a dimensionless radius of 1). The three methods also showed a ZnO minimum at the same respective location as the Zn maximum. Yet, the ZnO profiles closer to the pin showed different overall shapes, caused by the choice of the calculation method.

Assessment of the Pseudo-Cylindrical Coordinate Method

The differences in the profiles in Figure 7b supported the need for the pseudo-cylindrical analysis. For anodes with current collecting pins that were significantly off-center or separators

https://doi.org/10.1021/acsmeasuresciau.3c00015
ACS Meas. Sci. Au 2023, 3, 344−354

that were very squared, the radial phase volume profiles obtained were dependent on the way in which they were calculated. It was therefore critical that the pseudo-cylindrical method was developed to determine the radial profiles within these batteries, regardless of the location of the current collecting pin or the shape of the separator. This was not only to compare radial dependencies across batteries discharged using different protocols but also necessary to compare experimental results with model predictions.

In this work, we introduced the pseudo-cylindrical coordinate method, which is different from defining a center based on a reference, for example, the anode separator or current collecting pin. This method is superior because it results in good θ symmetry for real-world batteries analyzed by CT. Since 1D battery models assume θ symmetry, this provides a method to average CT results for comparison to a model.

Considering that there were three distinct ways of determining the radial position of a given voxel, sometimes producing different radial profiles, we set out to determine which method was most effective overall. Since θ symmetry was assumed in this system, the radial profiles produced by the three methods could be compared based on their display of symmetry in the θ dimension. It is important to note that there were two ways of computing θ, where either the center of the separator or the current collecting pin was used as the reference point, defined by eqs 5 or 6, respectively. Each method for computing the radial profiles was more appropriately associated with one of the definitions of θ. Specifically, it was more appropriate to use θ_{sep} when computing the radial profile with the distance from the center of the anode based on the location of the separator, whereas θ_{pin} was more appropriate to use with the other two methods, as these methods were centered around the current collecting pin.

For each battery, the anode was divided into eight θ-slices of $\pi/4$ radians each. This is shown in Figure 8a for the same segmented anode as in Figure 6b. The slicing in this image was done with respect to the center pin, the position of which is shown by a dashed line. This positioning defines the origin of the pin-centered absolute method as well as the pseudo-cylindrical method. An analogous method with the center defined by the separator was used for the separator-centered absolute method. The human eye is very good at summarizing the radial material profiles observed: a crust of mostly ZnO was found at the outer edge of the anode; a region of mixed Zn and ZnO was found near the center pin; and in the middle, a region with a higher amount of undischarged Zn was seen. However, the faithful calculation of a 1D radial profile for each material required numerical assessment. For each of the three methods, we calculated the agreement between the radial profiles of the eight individual θ-slices and the overall radial profile of the entire anode. For the analysis, index i referred to the θ-slice (1−8, as seen in Figure 8a); index j referred to the calculated average for the entire z-slice; and index k referred to the radial position. For example, the radial profile of a given phase for slice i can be represented by a vector, ε_i, with each element, $\varepsilon_{i,k}$, along the radius of the anode being indexed by k.

Material profiles of ZnO for each θ slice of the anode in Figure 8a are shown in Figure 8b. The goal was to verify how faithfully each radial profile method represented the entire 3D volume. In other words, did the resulting 1D radial profile for each phase in the 3D volume have good agreement with the profiles of each θ-slice and each z-slice. The Euclidean distance, $D_{i,j}$, was used to quantify the difference between the radial profile of a θ-slice, ε_i, and the average radial profile, ε_j, for a z-slice analyzed using one of the methods displayed in Figure 5. Using eq 17, the Euclidean distances between the radial phase volume fractions obtained from each θ-slice in a z-slice (around 2π radians) were calculated for Zn, ZnO, and pore. The analysis then moved to the next z-slice. The Euclidean distances for each θ-slice of every z-slice were averaged to obtain a single scalar quantity. This value, the mean Euclidean distance, quantified the closeness between all θ-slices within the overall 3D volume for a given anode

$$D_{i,j} = \sqrt{\sum_k (\varepsilon_{i,k} - \varepsilon_{j,k})^2} \tag{17}$$

A smaller value of the mean Euclidean distance indicated a better averaging method. For comparison, the mean Euclidean distance was calculated using each radial method for a collection of 10 batteries tested by synchrotron CT. Results are shown in Figure 9. These results quantify the symmetry achieved for the entire 3D volume of each cell, using the pseudo-cylindrical method, as well as the other two absolute methods.

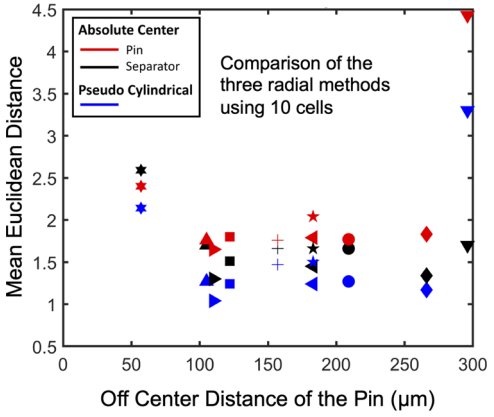

Figure 9. Mean Euclidean distances for the three methods of determining the radial phase volume profiles. The symbols used match those reported in Table 1.

The discharge histories of the 10 cells in Figure 9 are given in Table 1. Our purpose was not to compare cell performance but to assess how well the material profiles were averaged to single 1D radial distributions. The methods using an absolute center based on either the pin or separator are given in red and black, and the pseudo-cylindrical method is given in blue. Lower values of the mean Euclidean distance were desired. The mean Euclidean distances given in Figure 9 assessed how well each radial profile method represented the materials' radial distributions as single 1D profiles for each phase, which could be compared to the results of a 1D model. Of the 10 anodes, for 9 of them (90% of the cells compared), the pseudo-cylindrical method was the best due to the lower mean Euclidean distance. For cell #4, shown by ▼, the absolute method based on the separator was the best. The data in Figure 9 is plotted with the x-axis showing the off-center distance for the pin. However, the mean Euclidean distance was not found to be a strong function of this distance, meaning that while the off-center pin was one factor complicating the analysis, it was not the only contributor to variation in the

https://doi.org/10.1021/acsmeasuresciau.3c00015
ACS Meas. Sci. Au 2023, 3, 344−354

material profiles. The squared-off shape of the separator, which is a result of the manufacturing method, was another factor. For the single cell that did not show the best results for the pseudo-cylindrical method, the pin was highly off-center. The superior results of the absolute method based on the separator suggested that ionic conduction from the separator was the limiting factor in this cell. An electrochemical analysis of these effects will be the subject of future work.

For a large majority of the cells displayed in Figure 9, the method with the lowest mean Euclidean distance was that based on eq 16. Under the assumption of symmetry in θ, it was therefore concluded that calculating the radial profiles for cylindrical samples with an off-center reference point should be based on eq 16.

Effect of Visually Identifiable Features on Radial Results

As discussed above, an off-center pin or a squared separator could both cause issues with averaging material profiles. Another possible complication is defects. We now consider a battery that had relatively large variations in θ caused by a defect and observe how this impacted volume fraction profiles when averaged to a single 1D variation in r. Figure 10 shows a cross section of a partially discharged AA battery, taken to 1420 mA h DOD via a continuous discharge profile. This is cell #3, marked by ★ in Figure 9, which had a relatively large mean Euclidean distance compared to the other cells. The data was segmented into undischarged Zn (green), dense ZnO (pink), sparse ZnO (blue), and KOH-filled pore (black). A study of the ZnO phases with different densities has been published previously and is due to a difference in porosity that is below the resolution of the CT (<2.93 μm/voxel).[13] This sample had a relatively centered pin, which was only 57 μm off-center. However, the cell had a void defect near the pin that resulted in a far larger than normal variation in the θ-direction. In Figure 10, the data was divided into 8 θ-slices to produce 8 radial pore volume profiles for ZnO (both sparse and dense summed), Zn, and pore. These profiles are shown in Figure 11 for each anode slice. The void defect was in the lower right, significantly impacting radial slices 7 and 8. Neglecting these two slices, the radial profiles for each of the remaining slices followed the same general trend and implied symmetry in θ for this cell. Even for the slices with the void defect, the radial material profiles had the same appearance as the rest of the cell: undischarged Zn was located in the center of the anode at a distance from both the pin and separator; dense ZnO was generally found near the pin; and the more sparse, lower-density ZnO was found near the separator. Thus, we conclude that in cells with visible features affecting radial material profiles, the θ-slices involved may be removed from the average. The average would then be composed of only the slices without the defect.

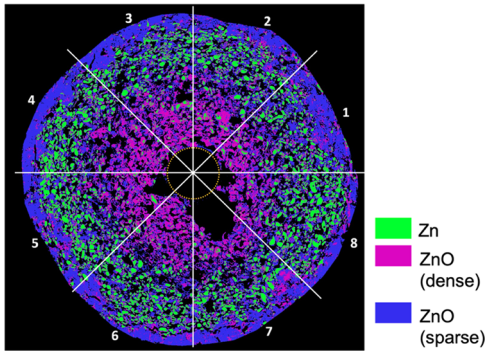

Figure 10. False-colored segmented cross section of the first cell in Figure 9 ★ continuously discharged to 1420 mA h (cell #3). The anode was divided into eight θ-slices along θ_{sep}, with a significant void defect in slices 7 and 8.

CONCLUSIONS

A pseudo-cylindrical analysis method was developed to measure radial phase volume fraction profiles from CT images of bobbin-type batteries. Due to the current collecting pin being off-center within the anode and/or the shape of the separator, this analysis had to consider the relative position between the current collecting pin and the outer edge of the anode. Three distinct methods for computing the radius were established and compared based on their apparent symmetry in

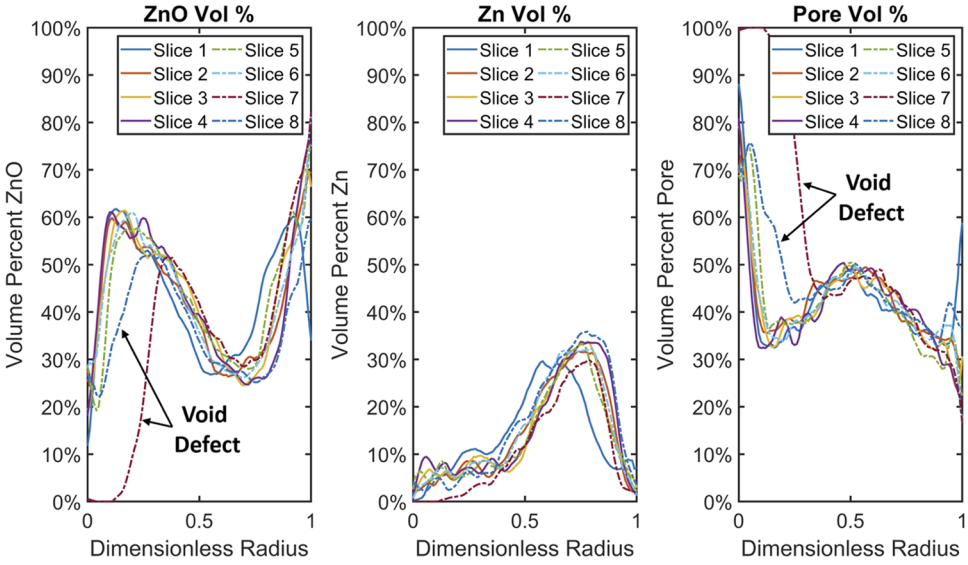

Figure 11. Smoothed radial phase volume fractions of the cell featured in Figure 10 (cell #3), with θ-slices 7 and 8 showing significant deviation in pore and ZnO content from the average θ-slice due to a manufacturing defect.

https://doi.org/10.1021/acsmeasuresciau.3c00015
ACS Meas. Sci. Au 2023, 3, 344−354

θ. It was found that the pseudo-cylindrical method based on the relative radial position between the current collecting pin and the outer edge of the anode showed greater symmetry in θ than when using the absolute distance from either the current collecting pin or the separator. This was true for 9 anodes compared out of a selection of 10 with varying discharge histories. Therefore, it is recommended that future analyses on bobbin-type batteries establish the radial profile based on the relative position between the current collecting pin and the separator, rather than the absolute distance from either of these.

AUTHOR INFORMATION

Corresponding Author

Joshua W. Gallaway − *Department of Chemical Engineering, Northeastern University, Boston, Massachusetts 02115, United States of America;* orcid.org/0000-0002-6798-7781; Email: j.gallaway@northeastern.edu

Authors

Dominick P. Guida − *Department of Chemical Engineering, Northeastern University, Boston, Massachusetts 02115, United States of America;* orcid.org/0000-0002-4744-6830

Alyssa M. Stavola − *Department of Chemical Engineering, Northeastern University, Boston, Massachusetts 02115, United States of America*

Andrew Chihpin Chuang − *Advanced Photon Source, Argonne National Laboratory, Lemont, Illinois 60439, United States of America*

John S. Okasinski − *Advanced Photon Source, Argonne National Laboratory, Lemont, Illinois 60439, United States of America*

Matthew T. Wendling − *Energizer Holdings, Inc., Westlake, Ohio 44145, United States of America*

Xiaotong H. Chadderdon − *Energizer Holdings, Inc., Westlake, Ohio 44145, United States of America*

Complete contact information is available at: https://pubs.acs.org/10.1021/acsmeasuresciau.3c00015

Author Contributions

CRediT: **Dominick P. Guida** investigation (lead), methodology (supporting), software (lead), visualization (lead), writing-original draft (equal), writing-review & editing (equal); **Alyssa M. Stavola** investigation (supporting); **Andrew Chihpin Chuang** investigation (supporting); **John S. Okasinski** investigation (supporting); **Matthew T. Wendling** methodology (supporting), writing-review & editing (supporting); **Xiaotong H. Chadderdon** methodology (supporting), writing-review & editing (supporting); **Joshua W. Gallaway** conceptualization (lead), methodology (lead), visualization (supporting), writing-original draft (equal), writing-review & editing (equal).

Notes

The authors declare no competing financial interest.

ACKNOWLEDGMENTS

D.P.G., A.M.S., and J.W.G. thank Energizer Holdings, Inc. for funding support. This research used resources of the Advanced Photon Source beamline 6-BM-A, a U.S. Department of Energy (DOE) Office of Science User Facility operated for the DOE Office of Science by Argonne National Laboratory under Contract No. DE-AC02-06CH11357. This work was completed in part using the Discovery cluster supported by Northeastern University's Research Computing team.

REFERENCES

(1) Osenberg, M.; Manke, I.; Hilger, A.; Kardjilov, N.; Banhart, J. An X-ray tomographic study of rechargeable Zn/MnO_2 batteries. *Materials* **2018**, *11*, No. 1486.

(2) Hack, J.; Patel, D.; Bailey, J. J.; Iacoviello, F.; Shearing, P. R.; Brett, D. J. In situ x-ray computed tomography of zinc−air primary cells during discharge: correlating discharge rate to anode morphology. *J. Phys.: Mater.* **2021**, *5*, No. 014001.

(3) Scharf, J.; Yin, L.; Redquest, C.; Liu, R.; Quinn, X. L.; Ortega, J.; Wei, X.; Wang, J.; Doux, J. M.; Meng, Y. S. Investigating Degradation Modes in Zn-AgO Aqueous Batteries with In Situ X-Ray Micro Computed Tomography. *Adv. Energy Mater.* **2021**, *11*, No. 2101327.

(4) Tariq, F.; Yufit, V.; Kishimoto, M.; Shearing, P.; Menkin, S.; Golodnitsky, D.; Gelb, J.; Peled, E.; Brandon, N. Three-dimensional high resolution X-ray imaging and quantification of lithium ion battery mesocarbon microbead anodes. *J. Power Sources* **2014**, *248*, 1014−1020.

(5) Su, Z.; Decencière, E.; Nguyen, T.-T.; El-Amiry, K.; De Andrade, V.; Franco, A. A.; Demortière, A. Artificial neural network approach for multiphase segmentation of battery electrode nano-CT images. *npj Comput. Mater.* **2022**, *8*, No. 30.

(6) Almeida, M. F.; Xará, S. M.; Delgado, J.; Costa, C. A. Characterization of spent AA household alkaline batteries. *Waste Manage.* **2006**, *26*, 466−476.

(7) Yeşiltepe, S.; Buğdaycı, M.; Yücel, O.; Şeşen, M. K. Recycling of alkaline batteries via a carbothermal reduction process. *Batteries* **2019**, *5*, No. 35.

(8) Lim, M. B.; Lambert, T. N.; Chalamala, B. R. Rechargeable alkaline zinc−manganese oxide batteries for grid storage: Mechanisms, challenges and developments. *Mater. Sci. Eng., R* **2021**, *143*, No. 100593.

(9) Scharf, J.; Chouchane, M.; Finegan, D. P.; Lu, B.; Redquest, C.; Kim, M.-c.; Yao, W.; Franco, A. A.; Gostovic, D.; Liu, Z.; Riccio, M.; Zelenka, F.; Doux, J.-M.; Meng, Y. S. Bridging nano-and microscale X-ray tomography for battery research by leveraging artificial intelligence. *Nat. Nanotechnol.* **2022**, *17*, 446−459.

(10) Bruck, A. M.; Kim, M. A.; Ma, L.; Ehrlich, S. N.; Okasinski, J. S.; Gallaway, J. W. Bismuth enables the formation of disordered birnessite in rechargeable alkaline batteries. *J. Electrochem. Soc.* **2020**, *167*, No. 110514.

(11) Gallaway, J. W.; Yadav, G. G.; Turney, D. E.; Nyce, M.; Huang, J.; Chen-Wiegart, Y.-c. K.; Williams, G.; Thieme, J.; Okasinski, J. S.; Wei, X.; Banerjee, S. An Operando Study of the Initial Discharge of Bi and Bi/Cu Modified MnO_2. *J. Electrochem. Soc.* **2018**, *165*, A2935−A2947.

(12) Mehta, S. A.; Bonakdarpour, A.; Wilkinson, D. P. Impact of cathode additives on the cycling performance of rechargeable alkaline manganese dioxide-zinc batteries for energy storage applications. *J. Appl. Electrochem.* **2017**, *47*, 167−181.

(13) Guida, D. P.; Chuang, A. C.; Okasinski, J. S.; Wendling, M. T.; Chadderdon, X. H.; Gallaway, J. W. Discharge intermittency considerably changes ZnO spatial distribution in porous Zn anodes. *J. Power Sources* **2023**, *556*, No. 232460.

(14) McLarnon, F. R.; Cairns, E. J. The Secondary Alkaline Zinc Electrode. *J. Electrochem. Soc.* **1991**, *138*, 645−664.

(15) Dirkse, T. P. Electrolytic oxidation of zinc in alkaline solutions. *J. Electrochem. Soc.* **1955**, *102*, 497−501.

(16) Dirkse, T. P.; Hampson, N. A. Anodic Behaviour of Zinc in Aqueous Koh Solution.1. Passivation Experiments at Very High Current Densities. *Electrochim. Acta* **1971**, *16*, 2049.

(17) Arise, I.; Kawai, S.; Fukunaka, Y.; McLarnon, F. R. Coupling Phenomena between Zinc Surface Morphological Variations and

Ionic Mass Transfer Rate in Alkaline Solution. *J. Electrochem. Soc.* **2013**, *160*, D66−D74.
(18) Liu, M. B.; Cook, G. M.; Yao, N. P. Passivation of Zinc Anodes in KOH Electrolytes. *J. Electrochem. Soc.* **1981**, *128*, 1663−1668.
(19) Horn, Q. C.; Shao-Horn, Y. Morphology and spatial distribution of ZnO formed in discharged alkaline Zn/MnO_2 AA cells. *J. Electrochem. Soc.* **2003**, *150*, A652−A658.
(20) Bockelmann, M.; Reining, L.; Kunz, U.; Turek, T. Electrochemical characterization and mathematical modeling of zinc passivation in alkaline solutions: A review. *Electrochim. Acta* **2017**, *237*, 276−298.
(21) Graae, K. V.; Norby, P. Time-and Space-Resolved In Situ X-ray Diffraction Study of Phase Transformations and Redistribution in Zn−Air Battery Anodes. *ACS Appl. Energy Mater.* **2022**, *5*, 11392−11401.
(22) Manke, I.; Banhart, J.; Haibel, A.; Rack, A.; Zabler, S.; Kardjilov, N.; Hilger, A.; Melzer, A.; Riesemeier, H. In situ investigation of the discharge of alkaline Zn-MnO_2 batteries with synchrotron x-ray and neutron tomographies. *Appl. Phys. Lett.* **2007**, *90*, No. 214102.
(23) Haibel, A.; Manke, I.; Melzer, A.; Banhart, J. In Situ Microtomographic Monitoring of Discharging Processes in Alkaline Cells. *J. Electrochem. Soc.* **2010**, *157*, A387−A391.
(24) Preefer, M. B.; Tanim, T. R.; Welborn, S. S.; Agyeman-Budu, D. N.; Dunlop, A. R.; Trask, S. E.; Dufek, E. J.; Jansen, A. N.; Weker, J. N. The Evolution of $LiNi_{0.5}Mn_{0.3}Co_{0.2}O_2$ Particle Damage from Fast Charging in Optimized, Full Li-Ion Cells. *J. Phys. Chem. C* **2022**, *126*, 21196−21204.
(25) Zielke, L.; Barchasz, C.; Waluś, S.; Alloin, F.; Leprêtre, J.-C.; Spettl, A.; Schmidt, V.; Hilger, A.; Manke, I.; Banhart, J.; et al. Degradation of Li/S battery electrodes on 3D current collectors studied using X-ray phase contrast tomography. *Sci. Rep.* **2015**, *5*, 1−12.
(26) Dixit, M. B.; Verma, A.; Zaman, W.; Zhong, X.; Kenesei, P.; Park, J. S.; Almer, J.; Mukherjee, P. P.; Hatzell, K. B. Synchrotron imaging of pore formation in Li metal solid-state batteries aided by machine learning. *ACS Appl. Energy Mater.* **2020**, *3*, 9534−9542.
(27) Jiang, Z.; Li, J.; Yang, Y.; Mu, L.; Wei, C.; Yu, X.; Pianetta, P.; Zhao, K.; Cloetens, P.; Lin, F.; Liu, Y. Machine-learning-revealed statistics of the particle-carbon/binder detachment in lithium-ion battery cathodes. *Nat. Commun.* **2020**, *11*, No. 2310.
(28) Boyce, A. M.; Martínez-Pañeda, E.; Wade, A.; Zhang, Y. S.; Bailey, J. J.; Heenan, T. M.; Brett, D. J.; Shearing, P. R. Cracking predictions of lithium-ion battery electrodes by X-ray computed tomography and modelling. *J. Power Sources* **2022**, *526*, No. 231119.
(29) Lu, X.; Bertei, A.; Finegan, D. P.; Tan, C.; Daemi, S. R.; Weaving, J. S.; O'Regan, K. B.; Heenan, T. M.; Hinds, G.; Kendrick, E.; et al. 3D microstructure design of lithium-ion battery electrodes assisted by X-ray nano-computed tomography and modelling. *Nat. Commun.* **2020**, *11*, No. 2079.
(30) Blazek, P.; Westenberger, P.; Erker, S.; Brinek, A.; Zikmund, T.; Rettenwander, D.; Wagner, N. P.; Keckes, J.; Kaiser, J.; Kazda, T.; et al. Axially and radially inhomogeneous swelling in commercial 18650 Li-ion battery cells. *J. Energy Storage* **2022**, *52*, No. 104563.
(31) Willenberg, L.; Dechent, P.; Fuchs, G.; Teuber, M.; Eckert, M.; Graff, M.; Kürten, N.; Sauer, D. U.; Figgemeier, E. The development of jelly roll deformation in 18650 lithium-ion batteries at low state of charge. *J. Electrochem. Soc.* **2020**, *167*, No. 120502.
(32) Stavola, A. M.; Sun, X.; Guida, D. P.; Bruck, A. M.; Cao, D.; Okasinski, J. S.; Chuang, A. C.; Zhu, H.; Gallaway, J. W. Lithiation Gradients and Tortuosity Factors in Thick NMC111-Argyrodite Solid-State Cathodes. *ACS Energy Lett.* **2023**, *8*, 1273−1280.
(33) Nguyen, T.-T.; Demortière, A.; Fleutot, B.; Delobel, B.; Delacourt, C.; Cooper, S. J. The electrode tortuosity factor: why the conventional tortuosity factor is not well suited for quantifying transport in porous Li-ion battery electrodes and what to use instead. *npj Comput. Mater.* **2020**, *6*, No. 123.
(34) Castro, M. T.; Del Rosario, J. A. D.; Ocon, J. D. Energy Density Optimization in a Primary Alkaline Battery using Multiphysics Modeling. *Chem. Eng. Trans.* **2022**, *94*, 301−306.
(35) Podlaha, E. J.; Cheh, H. Y. Modeling of Cylindrical Alkaline Cells. 6. Variable Discharge Conditions. *J. Electrochem. Soc.* **1994**, *141*, 28−35.
(36) Podlaha, E. J.; Cheh, H. Y. Modeling of Cylindrical Alkaline Cells. 5. High Discharge Rates. *J. Electrochem. Soc.* **1994**, *141*, 15−27.
(37) Sunu, W. G.; Bennion, D. Transient and Failure Analyses of the Porous Zinc Electrode: I. Theoretical. *J. Electrochem. Soc.* **1980**, *127*, 2007−2016.
(38) Dowd, B. A.; Campbell, G. H.; Marr, R. B.; Nagarkar, V. V.; Tipnis, S. V.; Axe, L.; Siddons, D. P. *Developments in synchrotron x-ray computed microtomography at the National Synchrotron Light Source*, Developments in X-ray Tomography II, SPIE, 1999; pp 224−236.
(39) Nock, R.; Nielsen, F. Statistical region merging. *IEEE Trans. Pattern Anal. Mach. Intell.* **2004**, *26*, 1452−1458.

https://doi.org/10.1021/acsmeasuresciau.3c00015
ACS Meas. Sci. Au 2023, 3, 344−354